

Characterizing decoherence rates of a superconducting qubit by direct microwave scattering

Yong Lu,^{1,*} Andreas Bengtsson,¹ Jonathan J. Burnett,^{1,2} Emely Wiegand,¹ Baladitya Suri,^{1,3} Philip Krantz,¹ Anita Fadavi Roudsari,¹ Anton Frisk Kockum,¹ Simone Gasparinetti,¹ Göran Johansson,¹ and Per Delsing^{1,†}

¹*Department of Microtechnology and Nanoscience (MC2),*

Chalmers University of Technology, SE-412 96 Göteborg, Sweden

²*National Physical Laboratory, Hampton Road, Teddington, Middlesex, TW11 0LW, United Kingdom*

³*Indian Institute of Science, Department of Instrumentation and Applied Physics, Bangalore 560012, India*

We experimentally investigate a superconducting qubit coupled to the end of an open transmission line, in a regime where the qubit decay rates to the transmission line and to its own environment are comparable. We perform measurements of coherent and incoherent scattering, on- and off-resonant fluorescence, and time-resolved dynamics to determine the decay and decoherence rates of the qubit. In particular, these measurements let us discriminate between non-radiative decay and pure dephasing. We combine and contrast results across all methods and find consistent values for the extracted rates. The results show that the pure dephasing rate is one order of magnitude smaller than the non-radiative decay rate for our qubit. Our results indicate a pathway to benchmark decoherence rates of superconducting qubits in a resonator-free setting.

I. INTRODUCTION

Superconducting circuits are promising building blocks for implementing quantum computers [1–3]. In those devices, the key elements are superconducting artificial atoms made by Josephson junctions which induce a strong and engineerable nonlinearity. Such artificial atoms are also used in the field of superconducting waveguide quantum electrodynamics (waveguide QED) [4, 5], where they interact with a continuum of light modes in a 1D waveguide. In the past decade, many quantum effects from atomic physics and quantum optics have been demonstrated in waveguide QED, e.g., the Mollow triplet [6], giant cross-Kerr effect [7] and cooperative effects [5, 8, 9]. Other recent experiments have shown phenomena which are currently beyond the reach of atomic physics, such as ultra-strong [10, 11] and superstrong coupling [12] between light and matter. Waveguide QED is also an enabling quantum technology. One of the key applications is to generate [13–19] and detect [4, 20–26] single photons. It has been proposed to use waveguide QED to create bound states [27–29] and implement quantum computers [30–32].

The performance of quantum computers and waveguide-QED devices is often limited by the coherence of the Josephson circuits. For example, the efficiency of producing and detecting single photons, the lifetime of bound states, and the fidelity of logical gates can all be improved by enhancing the coherence. In a waveguide-QED setup, decoherence can be due to decay into the waveguide, pure dephasing, and non-radiative decay rate into other modes. However, the rates for pure dephasing and non-radiative decay are typically

not explored separately. An understanding of which one is dominant will give an insight into the decoherence mechanisms, and thus how device performance can be improved.

In this work, we probe a superconducting transmon qubit coupled directly to the end of an open transmission line. In previous realizations [6–8, 33–35], the coupling rates were much larger than intrinsic decoherence mechanisms of the qubit, so the effects of non-radiative decay and pure dephasing were small and could not be well characterized. Here, we investigate a qubit whose radiative decay rate into the transmission line is larger than, yet comparable to, other decoherence mechanisms. This allows us to explore the pure dephasing rate Γ_ϕ , the radiative decay rate Γ_r from the capacitive coupling to the waveguide, and the non-radiative decay rate Γ_n . The total relaxation and decoherence rates are given by $\Gamma_1 = \Gamma_r + \Gamma_n$ and $\Gamma_2 = \Gamma_1/2 + \Gamma_\phi$, respectively. We demonstrate different methods to extract the different rates and find consistent results. In contrast to the results in circuit QED [36–40], our methods enable the evaluation of the decoherence of qubits over a broad range of frequencies, and provide a pathway to investigate Josephson junctions or superconducting quantum interference devices (SQUIDs) without any resonator. In addition, we also consider it important to study Γ_n and Γ_ϕ separately. For instance, this could help to improve the Purcell enhancement factor, $\frac{\Gamma_r}{\Gamma_n + 2\Gamma_\phi}$, in devices such as that presented in Ref. [9]. Moreover, the spontaneous-emission factor β , which is customarily quoted in other waveguide-QED platforms [41–44] is also related to Γ_n , namely, $\beta = \frac{\Gamma_r}{\Gamma_r + \Gamma_n}$ in our case.

The paper is structured as follows: in Sec. II, we characterize the coherent scattering of the device and obtain the radiative decay rate and the decoherence rate of the qubit as a reference for later measurements. In Sec. III, we exploit the fluorescence of the qubit under coherent excitation to find the non-radiative decay rate

* e-mail: yongl@chalmers.se

† e-mail: per.delsing@chalmers.se

and the pure dephasing rate. The resonance fluorescence spectrum at strong driving develops into the Mollow triplet [45], which has been widely used to probe quantum properties in systems based on superconducting qubits such as coherence [6, 8] and vacuum squeezing [46]. The resonance spectrum is symmetric around the central peak. However, if pure dephasing exists, the off-resonant spectrum becomes asymmetric, something which has been studied experimentally in quantum dots [47, 48]. We take advantage of this fact to extract the pure dephasing rate. In Sec. IV, we measure the non-radiative decay rate under a continuous coherent drive, where coherently and incoherently scattered photons provide information about the different decay channels. In Sec. V, we apply a pulse to the qubit to both obtain the decay rates and find the stability of the qubit frequency and coherence as a function of time. In contrast to other methods, we use the phase information of emitted photons from the qubit to investigate the qubit-frequency stability in superconducting waveguide QED. Finally, in Sec. VI, we summarize the measured results and compare the advantages and disadvantages of the different methods.

II. DEVICE CHARACTERIZATION

The device used in our experiment [see Fig. 1(a)] is a magnetic-flux-tunable Xmon-type transmon qubit [51], capacitively coupled to the open end of a one-dimensional transmission line with characteristic impedance $Z_0 \simeq 50 \Omega$. The circuit is equivalent to an atom in front of a mirror in 1D space. The device is fabricated from aluminum on a silicon substrate using the same fabrication recipe as in Ref. [38]. We denote $|0\rangle$, $|1\rangle$ and $|2\rangle$ as ground state, first and second excited states of the qubit, respectively. The $|0\rangle - |1\rangle$ transition energy is $\hbar\omega_{01} \approx \sqrt{8E_J(\Phi)E_C} - E_C$, where $E_C = e^2/(2C_\Sigma)$ is the charging energy, e is the elementary charge, C_Σ is the total capacitance of the qubit, and $E_J(\Phi)$ is the Josephson energy. The Josephson energy can be tuned from its maximum value $E_{J,max}$ by an external magnetic flux Φ using a coil: $E_J(\Phi) = E_{J,max}|\cos(\pi\Phi/\Phi_0)|$, where $\Phi_0 = h/(2e)$ is the magnetic flux quantum.

Figure 1(a) illustrates the simplified experimental setup for measuring the reflection coefficient of a probe signal from a vector network analyzer (VNA) after interacting with the qubit. The probe signal at frequency ω_{pr} and a pump at frequency ω_p are combined and attenuated before being fed into the transmission line. Then, the VNA receives the reflected signal to determine the complex reflection coefficient.

Figure 1(b) shows the magnitude of the reflection coefficient, $|r|$, for a weak probe (with an intensity $\Omega_{pr} < \Gamma_2$) as a function of the external flux Φ . We use two-tone spectroscopy to determine the anharmonicity of the qubit, $\alpha = (\omega_{12} - \omega_{01})/\hbar$, where ω_{12} is the frequency of the $|1\rangle \leftrightarrow |2\rangle$ transition. Specifically, we apply a strong

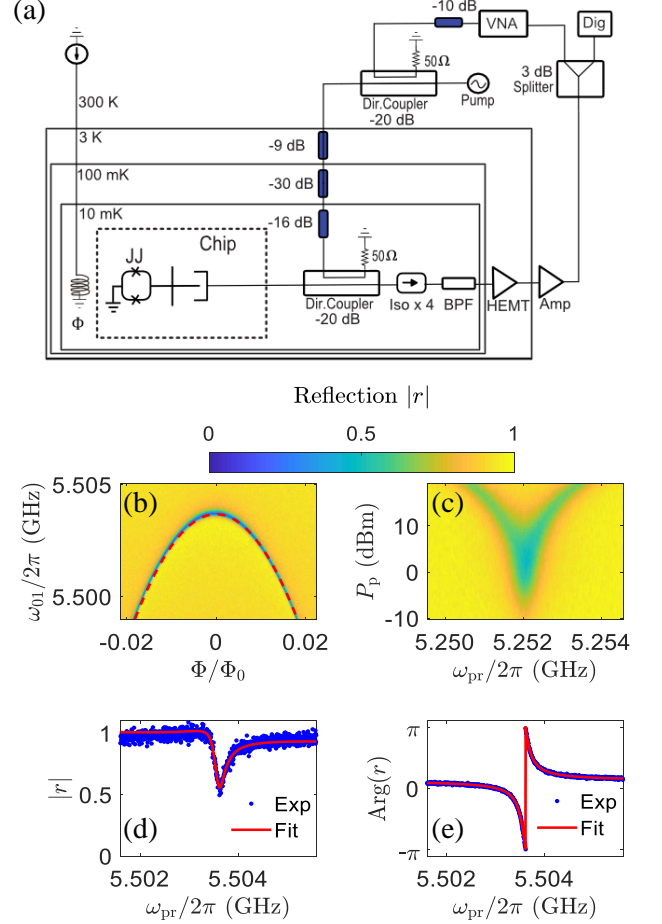


FIG. 1. Measurement setup and spectroscopy of a transmon qubit. (a) A simplified schematic of the setup and experimental device. JJ, Iso, BPF, HEMT, Amp and Dig denote Josephson junctions, isolators, a bandpass filter, a high electron mobility transistor amplifier, room-temperature amplifiers, and a digitizer, respectively. In the dashed box is our chip, where a qubit is formed by a cross-shaped island connected to the ground plane via two Josephson junctions. The qubit is located at the end of an open transmission line with a coplanar geometry. A weak probe signal generated by a VNA is combined with a pump, using a directional coupler, fed through attenuators to the qubit in a cryostat cooled to 10 mK. The reflected signal is then measured by the VNA. (b) Single-tone spectroscopy. The magnitude of the reflection coefficient r is measured as a function of the external flux Φ and probe frequency ω_{pr} . The red dashed curve is a fit for the qubit frequency ω_{01} . (c) Two-tone spectroscopy. A strong pump is applied to the $|0\rangle - |1\rangle$ transition in order to saturate the population of the first excited state of the qubit. When the applied weak probe is on resonance with the $|1\rangle - |2\rangle$ transition, the signal is either scattered incoherently or lost into the environment, leading to a reflection-coefficient magnitude less than unity. At higher pump power, the Autler-Townes splitting is observed [49]. From this, we obtain the qubit anharmonicity $\alpha = -252$ MHz. (d) and (e) show the magnitude and phase response of the qubit at $\Phi = 0$ under weak probing. Red lines are the corresponding fits using the circle fit technique from Ref. [50].

pump (with an intensity $\Omega_p \gg \Gamma_2$) at ω_{01} to saturate the $|0\rangle - |1\rangle$ transition and measure the reflection coefficient as a function of probe frequency. The result is shown in Fig. 1(c): a dip appears in the reflection at $\omega_{pr} = \omega_{12}$ due to the photon scattering from the $|1\rangle - |2\rangle$ transition. From Fig. 1(b) and (c), we find $E_C \approx \alpha = 252$ MHz, and then, $E_{J,max} = 16.56$ GHz by fitting the data in Fig. 1(b) to the equation between the qubit frequency and the external flux mentioned previously. In order to obtain the radiative decay and decoherence rates, we perform single-tone spectroscopy with a weak probe ($\Omega_{pr} \ll \Gamma_2$). Figure 1(d) and (e) are the corresponding magnitude and phase response of r , where we obtain $\Gamma_r/2\pi = 227$ kHz and $\Gamma_2/2\pi = 141$ kHz by using the circle fit technique from Ref. [50].

III. ATOMIC FLUORESCENCE

Even though a measurement of the reflection coefficient can give the decoherence and radiative decay rates, it cannot distinguish between pure dephasing and non-radiative decay. In order to distinguish them, we study the atomic fluorescence for different pump intensities and frequencies. For this measurement, the VNA is turned off, the pump is used to drive the system, another 50 dB of attenuation is added between the directional coupler and the pump, and the output signal is sampled by a digitizer [compare Fig. 1(a)]. When the qubit is pumped, its state evolves at a Rabi frequency Ω . With a Rabi frequency much larger than the natural linewidth of the qubit ($\Omega \gg \Gamma_2$), the energy levels of the qubit become dressed, leading to three distinct spectral components known as the Mollow triplet [45]. In particular, the spectrum contains the elastic 'Rayleigh' line in the middle in which the scattered wave has the same frequency as the incident wave, with two inelastic sidebands positioned symmetrically on both sides of the center peak.

A. On-resonant Mollow triplet

Under resonant continuous microwave excitation ($\Delta = \omega_p - \omega_{01} = 0$), as shown in Fig. 2(a), the splitting between the sidebands and the central peak increases as the pump power P_p . The splitting equals the Rabi frequency and obeys $\Omega = 2\sqrt{A\Gamma_r P_p/(\hbar\omega_{01})}$. By fitting the extracted Rabi splitting $|\Omega|$ in Fig. 2(b), and using Γ_r from the previous measurement in Sec. II, we extract a total attenuation $A = -145$ dB of which about -125 dB attenuation is from attenuators and directional couplers, -7 dB from an Eccosorb filter and the rest is due to cable loss. This allows us to renormalize all applied powers to either the power at the qubit, or the corresponding Rabi frequency. The total gain in the output line of the measurement setup can be calibrated by tuning the qubit away and measuring the power at the output port at room temperature. This results in a total gain $G =$

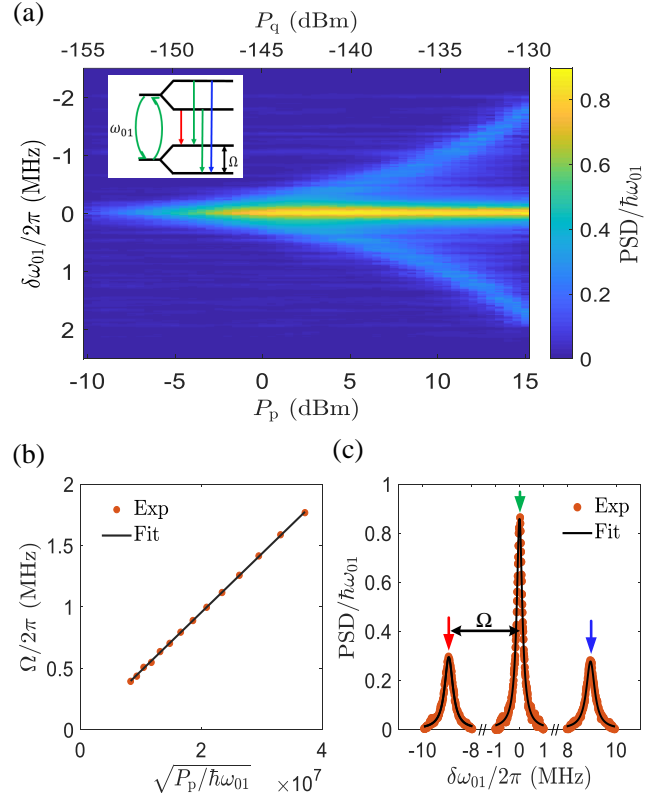


FIG. 2. Power spectral density (PSD) of the on-resonant Mollow triplet from the atomic fluorescence. (a) Resonant fluorescence emission spectrum as a function of the pump power and detuning of the detected radiation, $\delta\omega_{01} = \omega - \omega_{01}$. P_p is the power from the RF source while P_q is the corresponding power on the qubit. Inset: a schematic of the triplet transitions in the dressed-state picture, where the qubit energy levels split by Ω due to strong driving, creating three transitions with frequencies $\omega_{01} - \Omega$, ω_{01} and $\omega_{01} + \Omega$. (b) Rabi splitting Ω (dots) vs drive amplitude, extracted from (a). The black line is the linear fit to obtain the attenuation in the input line which is $A = -145$ dB. (c) Power spectral density at -116 dBm power at the sample. The black lines are individual fits to the linewidths of the three peaks, yielding $\Gamma_2/2\pi = 141 \pm 2$ kHz and $\Gamma_1/2\pi = 276 \pm 5$ kHz. The arrows correspond to the transitions in the inset of (a).

115 dB, of which approximately 44 dB gain comes from a high electron mobility transistor (HEMT) amplifier, and the rest is from the room temperature amplifiers and the pre-amplifiers of the digitizer.

The Rabi rate can be made much larger than all the decay rates of the qubit ($\Omega \gg \Gamma_1, \Gamma_2$). Consequently, the overlap in the frequency domain between the sideband emission and the central peak becomes negligible. In Fig. 2(c), we use an input power to the qubit $P_q \approx -116$ dBm, equivalent to $\Omega/2\pi \approx 9$ MHz. The incoherent part of the corresponding power spectral density (PSD)

is given by

$$S_i(\omega) \approx \frac{1}{2\pi} \frac{\hbar\omega_{01}\Gamma_r}{4} \left\{ \frac{\Gamma_s}{(\delta\omega_{01} + \Omega)^2 + \Gamma_s^2} + \frac{2\Gamma_2}{\delta\omega_{01}^2 + \Gamma_2^2} + \frac{\Gamma_s}{(\delta\omega_{01} - \Omega)^2 + \Gamma_s^2} \right\}, \quad (1)$$

[see Eq. (A18) in Appendix A], where the half width at half maximum of the central peak and the sidebands are Γ_2 and $\Gamma_s = (\Gamma_1 + \Gamma_2)/2$, respectively. The solid curves in Fig. 2(c) are fits to Eq. (1) using that the PSD expressed in linear frequency is $2\pi S_i(\omega)$. We obtain $\Gamma_2/2\pi = 141 \pm 2$ kHz for the central peak, $\Gamma_{s,\text{red}}/2\pi = 210 \pm 3$ kHz and $\Gamma_{s,\text{blue}}/2\pi = 206 \pm 4$ kHz for sidebands. By taking the average of $\Gamma_{s,\text{red}}$ and $\Gamma_{s,\text{blue}}$, we obtain $\Gamma_1/2\pi = 275 \pm 7$ kHz. We note that the extracted $\Gamma_2/2\pi$ value is fully consistent with the result from the reflection-coefficient measurement in Sec. II. From that measurement, we also know $\Gamma_r/2\pi = 227 \pm 1$ kHz. Thus, we can now extract both the non-radiative decay rate, $\Gamma_n/2\pi = 48 \pm 7$ kHz, and the pure dephasing rate, $\Gamma_\phi/2\pi = 3 \pm 4$ kHz.

By integrating the PSD of each peak in the Mollow triplet we can compare their relative weights. After normalization with $\hbar\omega_{01}\Gamma_r$, the results are about 0.254, 0.116 and 0.124 for the middle peak, the red and blue sidebands, respectively. According to Eq. (1), we would expect these numbers to be 0.250, 0.125 and 0.125, respectively, for a fully saturated qubit.

B. Off-resonant Mollow triplet

We also study the off-resonant Mollow triplet at a variety of pump powers and frequency detunings between the pump and the qubit. In Fig. 3(a), the pump power at the qubit is swept from -150 dBm to -130 dBm at detuning $\Delta/2\pi = 790$ kHz. We find that the PSD is weaker than in the on-resonant case, implying that the qubit is less excited. In Fig. 3(b), as we sweep the frequency detuning between the pump and the qubit, the spectrum over 1 MHz bandwidth is nearly symmetric, so that the extracted pure dephasing rates by the off-resonant fluorescence are insensitive to the frequency detuning Δ . We can either choose a large Δ which will lead to a small excitation of the qubit, or a small Δ which results in an unresolved spectrum between the central peak and sidebands.

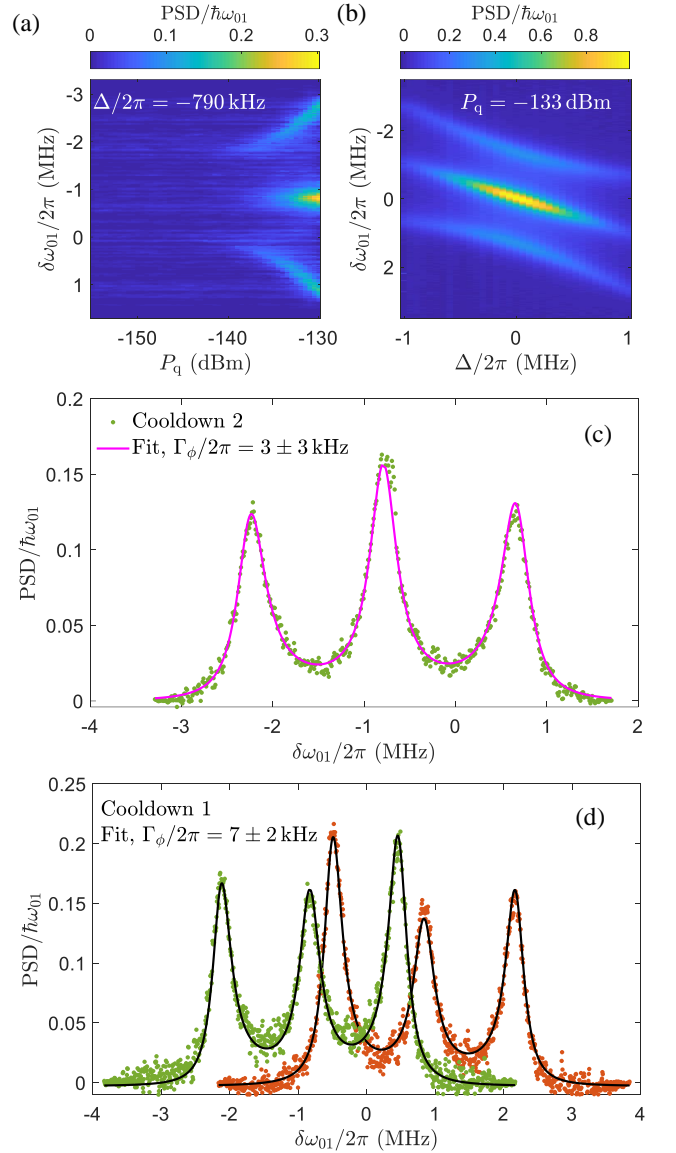


FIG. 3. Power spectral density of the off-resonant Mollow triplet from the atomic fluorescence. (a) Off-resonant fluorescence emission spectrum as a function of the pump power at the qubit. The frequency of the pump field is detuned by $\Delta = \omega_p - \omega_{01} = -2\pi * 790$ kHz from the qubit frequency. The Rabi splitting is increased with the input power. (b) Off-resonant fluorescence emission spectrum as a function of the frequency of the pump at $P_q = -133$ dBm. (c) Off-resonant PSD at $\Delta/2\pi = -790$ kHz (green dots) with $P_q = -133$ dBm. The solid curve is a fit to $\Gamma_1/2\pi = 275 \pm 6$ kHz and $\Gamma_\phi/2\pi = 3 \pm 3$ kHz. (d) Off-resonant PSD in a second cooldown at $\Delta/2\pi = 820$ kHz (brown dots), $\Delta/2\pi = -830$ kHz (green dots). A value of $\Gamma_\phi/2\pi = 7$ kHz gives a good fit to both traces (black).

Compared to the on-resonant case, the off-resonant Mollow triplet carries additional information in its sideband asymmetry and the approximation used in Eq. (1) is no longer valid. Therefore, the full expression for the PSD must be used, shown in Eq. (A16) in

TABLE I. Summary of the different rates extracted using different methods. The first method is a measurement of the reflection coefficient under a weak probe [Sec. II]. On-res.MT and Off-res.MT represent the on/off-resonant Mollow triplet from atomic fluorescence, respectively [Sec. III]. The energy loss is estimated by calibrating the input power and measuring both the coherent and incoherent power scattered by the atom [Sec. IV]. Finally, time resolved measurements of the decay from both a superposition state and the first excited state were used [Sec. V]. BW and T are the measurement bandwidth and the total measurement time, respectively, for each method.

Method	$\Gamma_r/2\pi$ kHz	$\Gamma_n/2\pi$ kHz	$\Gamma_\phi/2\pi$ kHz	$\Gamma_1/2\pi$ kHz	$\Gamma_2/2\pi$ kHz	BW MHz	T h
Reflection	227 (1)	-	-	-	141 (1)	4	3
On-res.MT	-	48 (7)	3 (4)	275 (7)	141 (2)	2	8
Off-res.MT	-	48 (6)	3 (3)	275 (6)	140 (3)	5	23
Scattering	229 (2)	49 (1)	1 (1)	278 (2)	140 (1)	5	63
SinglePoint	-	50 (3)	2 (2)	277 (2)	-	5	2
Dynamics	-	46 (11)	9 (5)	273 (11)	145 (1)	20	23

Appendix A which is an extension of Ref. [52]. The fit of the data in Fig. 3(c) to Eq. (A16) yields $\Gamma_\phi/2\pi = 3 \pm 3$ kHz (pink solid line). The symmetry of the sidebands around the central peak is due to the relatively small pure dephasing rate. In Fig. 3(d), the sample was measured in an earlier cooldown. There, we observed a larger asymmetry for both positive (green dots) and negative detunings (brown dots). In the case of positive detuning, the red sideband is closer to the qubit original frequency than the blue sideband, whereas the blue sideband is closer when the sign of the detuning is changed. We fit the two set of data simultaneously to obtain $2\pi * (7 \pm 2)$ kHz, which is slightly larger than the second cooldown. This is likely due to that we used only two isolators in the first cooldown, and four isolators in the second cooldown, leading to less thermal photons from the transmission line in the second case.

The mechanism by which the pure dephasing gives rise to an asymmetry in the Mollow triplet can be understood as follows (for details, see Appendix B). Relaxation from the qubit will cause transitions between dressed states $|n, \pm\rangle$ [see Fig. 4(a)] that contain different numbers n of drive photons. As shown in Fig. 4(b), these transitions will either be between or within the $+$ and $-$ subspaces. In equilibrium, if the pure dephasing rate is zero, the probabilities P_\pm for the system to be in these subspaces are given by the detailed-balance condition

$$\Gamma_{+-}P_+ = \Gamma_{-+}P_-, \quad (2)$$

i.e., the number of emitted photons causing transitions from $+$ to $-$ (the blue sideband) must equal the number of emitted photons causing transitions from $-$ to $+$ (the red sideband). However, the interaction causing pure dephasing has a non-zero matrix element for transitions between $|n, +\rangle$ and $|n, -\rangle$, which leads to a modified

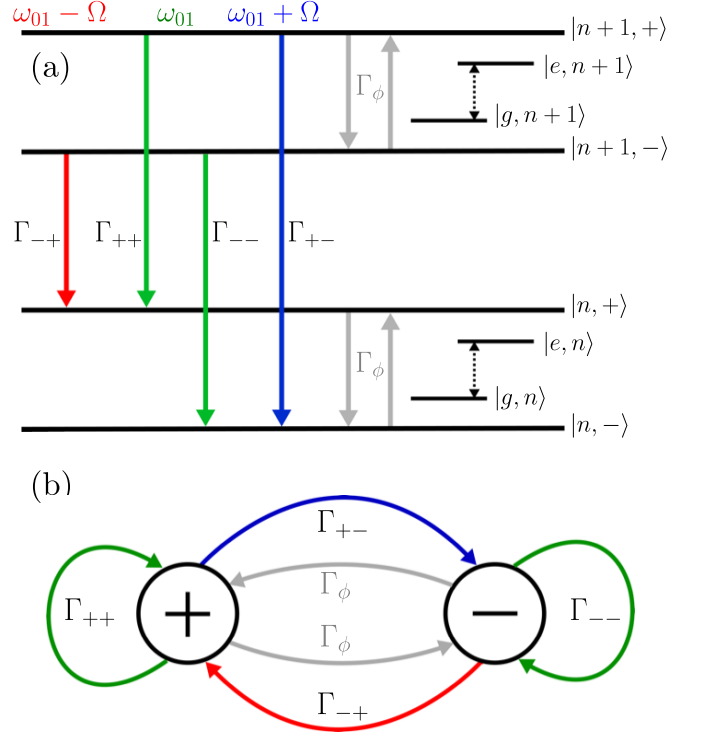


FIG. 4. Dressed states and transitions of the driven qubit. (a) Sketch of the dressed-state picture, including energies and transition rates. The states $|e, n\rangle$, $|g, n\rangle$, $|e, n+1\rangle$, and $|g, n+1\rangle$ are the bare states; the states $|n, \pm\rangle$ and $|n+1, \pm\rangle$ are the dressed states. (b) Transitions and transition rates between the $+$ and $-$ subspaces.

detailed-balance condition:

$$(\Gamma_{+-} + \Gamma_\phi)P_+ = (\Gamma_{-+} + \Gamma_\phi)P_-. \quad (3)$$

As Γ_ϕ increases, this will push the occupation probabilities towards $P_+ = P_-$. For off-resonant driving $\Gamma_{+-} \neq \Gamma_{-+}$ and thus the number of emitted photons in the two sidebands becomes different: $\Gamma_{+-}P_+ \neq \Gamma_{-+}P_-$. The larger number of photons will be emitted at the frequency corresponding to the larger of the two transition rates Γ_{+-} and Γ_{-+} ; from transition-matrix elements, this can be seen to be the frequency that is closer to the qubit frequency.

From Fig. 3(c), we have $\Gamma_1/2\pi = 275 \pm 6$ kHz and $\Gamma_2/2\pi = 140 \pm 3$ kHz. Again, from the measured radiative decay rate, by subtracting Γ_r from Γ_1 , we obtain $\Gamma_n/2\pi = 48 \pm 6$ kHz. Based on the results in this section, the on/off-resonant Mollow spectra allow us to extract the pure dephasing rate and non-radiative rate of a qubit. Specifically, for our qubit in this environment, we find that the non-radiative decay rate is one order of magnitude larger than the pure dephasing rate. Compared to the on-resonant Mollow triplet, the off-resonant Mollow triplet allows us to characterize the qubit decay rates at a lower pump power.

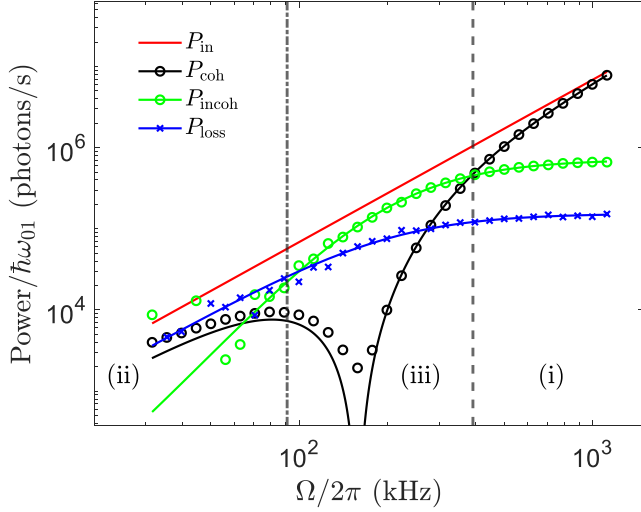


FIG. 5. Normalized powers as a function of Rabi frequency. The input power, P_{in} (red), representing the input photon flux at the qubit, is measured when the qubit is tuned away by the external flux. When the qubit is on resonance with the input signal, we have the coherent power, P_{coh} (black circles), consisting of photons reflected from either the qubit or the end of the transmission line. The qubit can also scatter photons incoherently, P_{incoh} (green circles), due to the decoherence of the qubit. Moreover, the excited qubit has some probability to release a photon to the environment resulting in the power loss, P_{loss} (blue crosses). The solid curves are fits to different types of the scattered powers. The dotted and dash-dotted lines separate the qubit response into three interesting regions (see more details in the text).

IV. PHOTON SCATTERING BY THE QUBIT

To verify the extracted decay rates above, we can also measure the power scattered by the qubit and the dissipated power due to the non-radiative decay channel directly. We normalize all the powers by the single-photon energy $\hbar\omega_{01}$. The pump is on resonance with the qubit. The output power then consists of a coherent part and an incoherent part, $P_{\text{out}} = P_{\text{coh}} + P_{\text{incoh}}$, where $P_{\text{coh}} = \frac{\Omega^2}{4\Gamma_r} (1 - \frac{\Gamma_1\Gamma_r}{\Omega^2 + \Gamma_2\Gamma_1})^2$ and $P_{\text{incoh}} = \frac{\Gamma_r}{2} \frac{\Omega^2(\Gamma_1\Gamma_2 + \Omega^2)}{(\Gamma_1\Gamma_2 + \Omega^2)^2}$ (see Appendix D).

For our qubit, the pure dephasing rate was verified to be around 3 kHz, i.e., much less than other rates and therefore negligible, so, the expression for the incoherent power can be further simplified to $P_{\text{incoh}} \simeq 2\Gamma_r\rho_{11}^2$, where ρ_{11} is the population of the first excited state of the qubit. In this cover, the expression for the dissipated power due to the non-radiative decay is then $P_{\text{loss}} = \Gamma_n\rho_{11} = \Gamma_n \frac{\Omega^2}{2(\Gamma_1\Gamma_2 + \Omega^2)}$.

Experimentally, we use about 4.2×10^9 averages to measure all the powers. We denote the measured voltage V , the system noise N , and the pump power P_{in} . The subscripts “off” and “on” used in the following contexts mean that the qubit is off/on resonance with the pump,

respectively. When the qubit is tuned away, it is off-resonant with the pump; we will have $P_{\text{in}} = \langle V \rangle_{\text{off}}^2$ because of the coherence of the pump. Besides the pump power, the system noise will also make a contribution to the total measured power, $P_{\text{in}}^{\text{meas.}}$. Therefore, we have $P_{\text{in}}^{\text{meas.}} = \langle V^2 \rangle_{\text{off}} = P_{\text{in}} + N$. When instead the qubit is on resonance with the pump, the total measured output power $P_{\text{out}}^{\text{meas.}} = \langle V^2 \rangle_{\text{on}} = P_{\text{out}} + N$, where $P_{\text{coh}} = \langle V \rangle_{\text{on}}^2$ (black circles). Therefore, P_{loss} (blue crosses) is obtained by taking $P_{\text{loss}} = P_{\text{in}}^{\text{meas.}} - P_{\text{out}}^{\text{meas.}} = P_{\text{in}} - P_{\text{out}}$ with $P_{\text{incoh}} = P_{\text{in}} - P_{\text{coh}} - P_{\text{loss}}$ (green circles). Figure 5 shows all the types of measured power as a function of the Rabi frequency. There, we find three interesting regions:

- (i) At high input power, when $\Omega > (1 + \frac{1}{\sqrt{2}})\Gamma_r = 2\pi * 391$ kHz, to the right of the dashed line in Fig. 5, the qubit starts to be saturated. The outgoing field is then mainly coherent from the pump itself. By increasing the input power further, the qubit is completely saturated, leading to $P_{\text{in}} \approx P_{\text{coh}} \approx \frac{\Omega^2}{4\Gamma_r}$, $P_{\text{incoh}} \approx \frac{\Gamma_r}{2}$ and $P_{\text{loss}} \approx \frac{\Gamma_n}{2}$. In this case, almost all the incoming photons are reflected by the mirror.
- (ii) In the low-power region ($\Omega < \sqrt{\frac{\Gamma_1\Gamma_2\Gamma_n}{\Gamma_r}} = 2\pi * 91$ kHz derived from $P_{\text{incoh}} = P_{\text{loss}}$, to the left of the dash-dotted line), the scattering process is dominated by the interaction between the qubit and the incoming photons. The incoherent scattering is proportional to ρ_{11}^2 whereas the power loss depends linearly on the excitation probability. Therefore, the incoherent power can be less than the power loss when $\rho_{11} < \frac{\Gamma_n}{2\Gamma_r} \approx 0.11$. Besides the incoherent photons, there is a small coherent scattering by the qubit. Compared to the loss, the coherent power is smaller if the non-radiative decay is large enough, namely if $\Gamma_n > \frac{\Gamma_1(\Gamma_r - \Gamma_2)^2}{2\Gamma_r\Gamma_2} \approx 2\pi * 34$ kHz.
- (iii) In the intermediate-power region where $\sqrt{\frac{\Gamma_1\Gamma_2\Gamma_n}{\Gamma_r}} < \Omega < (1 + \frac{1}{\sqrt{2}})\Gamma_r$, both the mirror and the qubit make substantial contributions to the scattering process. The photons reflected by the mirror interfere destructively with those scattered by the qubit, resulting in a suppression of the coherent part of the output field. In particular, the dip around $\Omega/2\pi \approx 160$ kHz in the coherent power appears due to the fully destructive interference. In addition, the qubit excitation is not small anymore and the incoherent power is larger than the loss because $\Gamma_r > \Gamma_n$. We note that this region can be non-existent when either the non-radiative decay or the pure dephasing is sufficiently large.

We also fit the data in Fig. 5 to obtain all the decay rates. The result for the incoherent power indicates $\Gamma_r/2\pi = 229 \pm 2$ kHz with $\Gamma_1\Gamma_2/4\pi^2 = 39590 \pm 211$ kHz² and $\Gamma_1\Gamma_\phi/4\pi^2 = 281 \pm 281$ kHz². From fits to the power

loss, we find $\Gamma_n/2\pi = 49 \pm 1 \text{ kHz}$ and $\Gamma_1\Gamma_2/4\pi^2 = 41260 \pm 4750 \text{ kHz}^2$. Therefore, with Γ_r and Γ_n , we obtain $\Gamma_1/2\pi = (\Gamma_n + \Gamma_r)/2\pi = 278 \pm 2 \text{ kHz}$. Then, $\Gamma_\phi/2\pi \simeq 1 \text{ kHz}$. The coherent power yields $\Gamma_r/2\pi = 229 \pm 2 \text{ kHz}$, $\Gamma_n/2\pi = 48 \pm 8 \text{ kHz}$ and $\Gamma_\phi/2\pi = 1 \pm 1 \text{ kHz}$. Then, with Γ_1 and Γ_ϕ , we have $\Gamma_2/2\pi = 140 \pm 1 \text{ kHz}$.

From the discussion on region (i), at the highest Rabi frequency $\Omega/2\pi = 1119 \text{ kHz}$ in Fig. 5, $\Gamma_n/\Gamma_r \approx P_{\text{loss}}/P_{\text{incoh}}$. Then, we obtain $\Gamma_n/\Gamma_r = [0.1971, 0.2385, 0.2227, 0.2297]$, by dividing the total measured data into four pieces. Combined with Γ_r from the reflection coefficient in Sec. II, we find $\Gamma_n/2\pi \approx 45, 54, 51, 52 \text{ kHz}$, respectively. The mean value is about 50 kHz with 3 kHz as the standard deviation. According to Eqs. (D4) and (D5) in Appendix D, as Γ_ϕ is small for our qubit, we have $\Gamma_n = 2P_{\text{loss}}(1 + \frac{\Gamma_1\Gamma_2}{\Omega^2})$ and $\Gamma_r \simeq 2P_{\text{incoh}}(1 + \frac{\Gamma_1\Gamma_2}{\Omega^2})^2$. Due to $\frac{\Gamma_1\Gamma_2}{\Omega^2} \approx 3\%$, $\Gamma_n \approx 2.06P_{\text{loss}}$ and $\Gamma_r \approx 2.12P_{\text{incoh}}$. Therefore, the estimated value for Γ_n has a systematic error of about 3% . Since $\Gamma_\phi = \Gamma_2 - \frac{\Gamma_r + \Gamma_n}{2}$ and $\Gamma_1 = \Gamma_r + \Gamma_n$, the pure dephasing and the non-radiative decay rates are $2\pi * (2 \pm 2) \text{ kHz}$ and $2\pi * (277 \pm 2) \text{ kHz}$, respectively. Additionally, because $P_{\text{loss}} = 2\pi * 0.0243 * 10^6$ and $P_{\text{incoh}} = 2\pi * 0.1056 * 10^6$, we have $\Gamma_n/2\pi \approx 49 \text{ kHz}$ and $\Gamma_r/2\pi \approx 224 \text{ kHz}$, respectively.

The results shown here agree well with the values from other sections in the paper, which implies that it is possible to take the Γ_r value from the reflection coefficient measurement as a reference for the Mollow triplet in order to separate the non-radiative decay rate and the pure dephasing rate.

V. TIME-RESOLVED DYNAMICS

All measurements described previously span time ranges from several hours to tens of hours. It is noteworthy that qubit decay rates extracted by different methods agree relatively well. However, the long duration means that any fluctuations of the decay rates are averaged out. Recently, several groups have characterized such fluctuations in circuit QED, using Rabi pulses, Ramsey interference measurements, and dispersive qubit readout [36–39]. To probe the decoherence of the qubit with a temporal resolution of 7 minutes, we prepare the qubit in a superposition of the ground and first-excited state and monitor its spontaneous emission into the waveguide by recording both quadratures of the output field with a digitizer as a complex trace in the time domain. We measure for $4.27 \times 10^5 \text{ s}$ (approximately 119 hours) with 975 repetitions, and each such trace has 2.30×10^6 averages.

After the 50 ns long $\pi/2$ -pulse, the qubit superposition state evolves in time τ as $\frac{1}{\sqrt{2}}(|0\rangle + e^{-\Gamma_2\tau - i\delta\omega_{01}\tau}|1\rangle)$ with $\delta\omega_{01} = \omega_{01} - \omega_{\text{pulse}}$. The emitted field carries information about the qubit operator $\langle\sigma_- \rangle = e^{-\Gamma_2\tau}e^{-i\delta\omega_{01}\tau}$, where the amplitude response and the phase response show the decoherence and the qubit frequency shift with τ ,

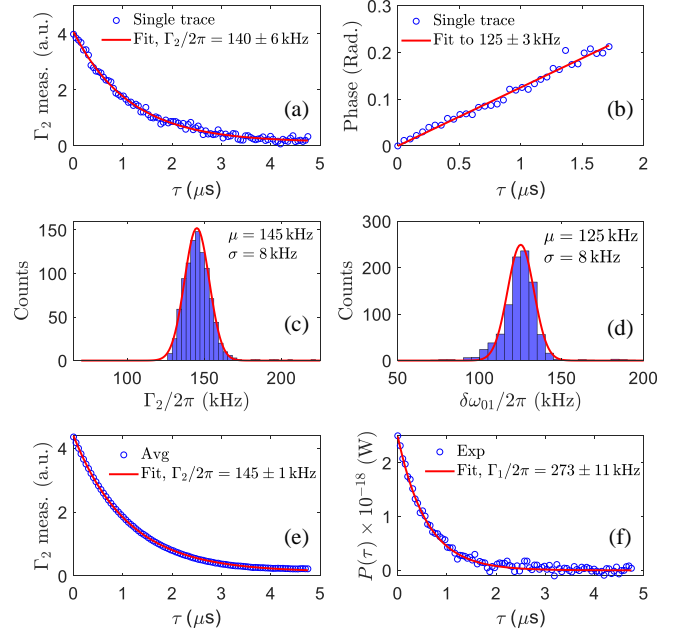


FIG. 6. Qubit dynamics to measure Γ_2 , Γ_1 and $\delta\omega_{01}/2\pi$. The magnitude response of the measured signal is proportional to the magnitude of the emission operator $\langle\sigma_- \rangle$ of the qubit while the phase response increases linearly with time as $\delta\omega_{01}\tau$. (a) A single trace of the magnitude response of Γ_2 measurements after a $\pi/2$ -pulse, showing the decoherence processes of the qubit within time τ . The data is fitted to an exponential decay. (b) The corresponding phase response from (a), showing that the phase of the emitted photon from the qubit evolves with a slope corresponding to the detuning $\delta\omega_{01}/2\pi = 125 \text{ kHz}$ where $\delta\omega_{01} = \omega_{01} - \omega_{\text{pulse}}$. (c) Histogram of Γ_2 from the magnitude response of the measurements from 975 traces, spanning $4.27 \times 10^5 \text{ s}$ (approximately 119 h). (d) Histogram of Γ_2 from the corresponding phase response of the measurements taken in (c). Both (c) and (d) have been fitted (solid line) to a Gaussian distribution with parameters shown. (e) The decay of the qubit state by averaging all the measured traces in (c) to extract the decoherence rate. (f) A π -pulse is applied to flip the qubit to the excited state with 1.92×10^9 averages, where $P(\tau)$ is the power emitted by the qubit at time τ after the pulse. By fitting the emitted power (blue circles) to an exponential decay, we extract $\Gamma_1/2\pi = 273 \pm 11 \text{ kHz}$. Except for the histograms, the error bars are for 95% confidence.

respectively.

Figures 6(a) and (b) show the magnitude and phase response of a single trace where the decay of the magnitude is fitted to an exponential curve and the phase of the photons emitted from the qubit grows linearly with time due to the free evolution of the qubit, where the slope determines $\delta\omega_{01}/2\pi = 125 \text{ kHz}$. Figures 6(c) and (d) are histograms of Γ_2 and $\delta\omega_{01}$ for all the repetitions. Both histograms can be fitted to a Gaussian with parameters shown in the figures. In comparison with the decoherence rates extracted from other measurements, we find that the standard deviation here is larger than the previously measured error bar.

This shows that the dynamics of the qubit on a short time differs slightly from that over a long measurement time. By taking the average of all the traces in Fig. 6(d), we fit to an exponential decay and get an averaged $\Gamma_2/2\pi = 145 \pm 1$ kHz.

To also study Γ_1 , we instead send a π -pulse to flip the qubit fully, and then measure the emission from the qubit. The corresponding output power, $P(\tau) = (\hbar\omega_{01}\Gamma_r/2)(1 + \langle\sigma_z\rangle)e^{-\Gamma_1\tau}$ [53] allows us to determine Γ_1 . The trace is measured with 1.92×10^9 averages, shown in Fig. 6(e). A fit to an exponential decay with $\Gamma_1/2\pi = 273 \pm 11$ kHz agrees well with the data. Combining these numbers with Γ_r from Sec. II, we can also calculate Γ_n and Γ_ϕ from these measurements. The resulting values can be seen in Table I.

VI. DISCUSSION AND CONCLUSION

We have shown several methods to determine different decay rates of a qubit placed in front of a mirror. In principle, these methods can also be used when the qubit couples to a transmission line without a mirror, except for the scattering method, where the corresponding measurement taken on both the input and output ports is required.

In our case, the measured rates are consistent between methods within the error bars of two standard deviation corresponding to 95% confidence. The results are summarized in Table I. The reflection measurement is the baseline to provide the value of Γ_r to extract the non-radiative decay rate of the qubit for measurements except for the scattering measurement. These different methods have advantages and disadvantages that we summarize below:

- (i) The fastest way to obtain the non-radiative decay rate is to send a strong pump on resonance with the qubit so that the central peak and the sidebands of the Mollow triplet do not overlap. The drawback is that the pump power needed here is much stronger than for the other methods and that may change the rates slightly.
- (ii) In the second method, we measure the off-resonant Mollow triplet by detuning the pump frequency slightly from the qubit frequency. The sidebands will be asymmetric around the central peak if the pure dephasing rate is non-negligible. In this case, only weak probe power is required. However, the corresponding measurement time is increased by almost a factor of three.
- (iii) The most accurate way to measure the non-radiative decay rate is to measure the difference between the input and output power, labelled as Scattering in Table I. Using this method, we can obtain not only the power loss but also the coherent and incoherent power scattered by the

qubit. However, the measurement time is much longer. In addition, the attenuation between the sample and the input line as well as the gain between the detector and the sample need to be calibrated at the beginning in order to get the absolute power values from the qubit. To simplify the measurement, as we discussed in Sec. III, we can use that when the pump saturates the qubit, we get $P_{\text{incoh}} \approx \frac{\Gamma_r}{2}$ and $P_{\text{loss}} \approx \frac{\Gamma_n}{2}$. Then, the ratio of the non-radiative decay rate to the radiative decay rate can be obtained from the ratio of the lost power to the incoherent power. Knowing the value of Γ_r from the reflection measurement, we can obtain the non-radiative decay rate. Therefore, in principle, we do not need to sweep the pump power as was done in Fig. 5. This simple way is labeled as SinglePoint in Table I.

- (iv) Finally, pulses can be applied to excite the qubit. Afterwards, the exponential decay of the emission and the emitted power trace from the qubit can be recorded to extract the total relaxation rate and the decoherence rate with a much larger measurement bandwidth. The distortion on the scattered photons due to the non-flat frequency response will affect the extracted values of the decay rates. This may be the reason why decay rates from this method are slightly different from those measured by other methods. However, the advantage of this method is that it allows us to study the short-time dynamics of the qubit.

The measurement time for these methods are from 2 hours to 63 hours. The coherent measurement is related to the first moment (amplitude) whereas other methods are related to the second moment (power). In order to estimate the system noise N , we measured the background PSD by turning the drive off (not shown) and comparing the result with the measurement of Fig. 2(c). We found $N \approx 49$ photons. However, we expect that using a quantum-limited Josephson traveling-wave amplifier [54] would reduce the system noise to about two photons. This would result in a reduction of the measurement time by factors of 5 and 25, respectively, for the coherent measurement and the other methods.

From the measured result, our qubit is T_1 -limited, i.e., the radiative decay dominates the interaction. However, the non-radiative decay rate is one order of magnitude larger than the pure dephasing rate. The corresponding spontaneous-emission factor is $\beta \approx 85\%$, which is typically close to 100% when we engineer the radiative decay much larger than the non-radiative decay. Therefore, to reduce the non-radiative decay rate will be the next step to improve the intrinsic coherence of our qubit. In addition, it is worthwhile to investigate why the non-radiative decay rate of our qubit is one order of magnitude larger than the qubit coupled to a resonator which was fabricated on the same wafer [38] in the future.

Our methods allow us to analyze all the decay channels

in detail. This will be useful to study and engineer decay channels of the qubit, which is the critical element in superconducting circuits. For example, engineering the decay channels can improve the quantum efficiency of generating single photons, which is set by $\Gamma_r/2\Gamma_2$. Also, the fidelity of detecting a single photon can be increased by extending the qubit coherence time. More importantly, compared to circuit QED where a resonator couples to a qubit dispersively, our study provides a straightforward way to investigate superconducting qubits, which are crucial elements in superconducting quantum computers.

VII. ACKNOWLEDGMENTS

We wish to express our gratitude to David Niepce and Marco Scigliuzzo for insightful discussions. We acknowledge financial support from the Knut, Alice Wallenberg Foundation, and the Swedish Research Council, and the EU-project OpenSuperQ.

Appendix A: Power Spectrum

Here, we follow the method in Ref. [52] to calculate our circuit model. Our qubit Hamiltonian is ($\hbar = 1$)

$$H = -\frac{\Delta}{2}\sigma_z + \frac{\Omega}{2}\sigma_x, \quad (\text{A1})$$

where $\Delta = \omega_p - \omega_{01}$; ω_p and ω_{01} are the pump frequency and the qubit $|0\rangle \leftrightarrow |1\rangle$ transition frequency, respectively.

The Lindblad master equation, describing the qubit dynamics with decoherence included, is given by

$$\frac{d}{dt}\rho = \mathcal{L}\rho = -i[H, \rho] + \mathcal{L}_\gamma\rho, \quad (\text{A2})$$

where the Liouvillian \mathcal{L}_γ is

$$\mathcal{L}_\gamma\rho = \Gamma_1 D[\sigma_-]\rho + \frac{\Gamma_\phi}{2} D[\sigma_z]\rho, \quad (\text{A3})$$

in which $D[c]\rho = c\rho c^\dagger - \frac{1}{2}(c^\dagger c\rho + \rho c^\dagger c)$.

In the frame rotating with ω_p , the corresponding equations of motion for $s_1(t) \equiv \rho_{10}(t) = \langle\sigma_-(t)\rangle e^{i\omega_p t}$ and $s_2(t) \equiv \rho_{11}(t) = \langle\sigma_+(t)\sigma_-(t)\rangle$ are obtained from Eq. (A2)

$$\frac{d}{dt} \begin{pmatrix} s_1 \\ s_1^* \\ s_2 \end{pmatrix} = M \begin{pmatrix} s_1 \\ s_1^* \\ s_2 \end{pmatrix} + B, \quad (\text{A4})$$

where

$$M = \begin{pmatrix} i\Delta - \Gamma_2 & 0 & i\Omega \\ 0 & -i\Delta - \Gamma_2 & -i\Omega \\ i\Omega/2 & -i\Omega/2 & -\Gamma_1 \end{pmatrix}, B = \begin{pmatrix} -i\Omega/2 \\ i\Omega/2 \\ 0 \end{pmatrix}. \quad (\text{A5})$$

Here, Γ_1 , Γ_ϕ , and $\Gamma_2 = \frac{1}{2}\Gamma_1 + \Gamma_\phi$ are the total relaxation rate of the qubit, the pure dephasing rate, and the decoherence rate, respectively.

The qubit reaches its stationary state for $t \gg \Gamma_{1,2}^{-1}$. The stationary values, $\bar{s}_1 = s_1(\infty)$ and $\bar{s}_2 = s_2(\infty)$, are

$$\bar{s}_1 = \frac{\Omega\Gamma_1(\Delta - i\Gamma_2)}{2(\Omega^2\Gamma_2 + \Gamma_1(\Delta^2 + \Gamma_2^2))}, \quad (\text{A6})$$

$$\bar{s}_2 = \frac{\Omega^2\Gamma_2}{2(\Omega^2\Gamma_2 + \Gamma_1(\Delta^2 + \Gamma_2^2))}. \quad (\text{A7})$$

To determine the two-time correlation function of the atom, three quantities are defined:

$$s_3(\tau) = \langle\sigma_+(t)\sigma_-(t+\tau)\rangle e^{i\omega_p\tau}, \quad (\text{A8})$$

$$s_4(\tau) = \langle\sigma_+(t)\sigma_+(t+\tau)\rangle e^{-i\omega_p(2t+\tau)}, \quad (\text{A9})$$

$$s_5(\tau) = \langle\sigma_+\sigma_+(t+\tau)\sigma_-(t+\tau)\rangle e^{-i\omega_p\tau}, \quad (\text{A10})$$

all of which are time-independent when stationary. From Eq. (A4), we have equations of motion for these quantities as

$$\frac{d}{dt} \begin{pmatrix} s_3 \\ s_4 \\ s_5 \end{pmatrix} = M \begin{pmatrix} s_3 \\ s_4 \\ s_5 \end{pmatrix} + B, \quad (\text{A11})$$

with initial values $s_3(0) = \bar{s}_2$ and $s_4(0) = s_5(0) = 0$. In the $\tau \rightarrow \infty$ limit, the stationary values are $\bar{s}_3 = |\bar{s}_1|^2$, $\bar{s}_4 = (\bar{s}_1^*)^2$, and $\bar{s}_5 = \bar{s}_1^*\bar{s}_2$. Using new variables, $\delta s_j(\tau) = s_j(\tau) - \bar{s}_j$ ($j = 3, 4, 5$), the above equations are rewritten as

$$\frac{d}{dt} \begin{pmatrix} \delta s_3 \\ \delta s_4 \\ \delta s_5 \end{pmatrix} = M \begin{pmatrix} \delta s_3 \\ \delta s_4 \\ \delta s_5 \end{pmatrix} = M * \delta S. \quad (\text{A12})$$

Here, $\delta s_3(\infty) = \delta s_4(\infty) = \delta s_5(\infty) = 0$. Taking the Fourier transforms of $\delta s_j(\tau)$ by $I_j(\omega) = \int_0^\infty d\tau e^{i(\omega - \omega_p)\tau} \delta s_j(\tau)$ with partial integration, we have

$$I(\omega) = [M + i(\omega - \omega_p)\mathbb{1}]^{-1} \left[\lim_{\tau \rightarrow \infty} \delta S(\tau) e^{i(\omega - \omega_p)\tau} - \delta S(0) \right]. \quad (\text{A13})$$

Because $\lim_{\tau \rightarrow \infty} \delta S(\tau) e^{i(\omega - \omega_p)\tau} = 0$,

$$I(\omega) = -[M + i(\omega - \omega_p)\mathbb{1}]^{-1} \delta S(0). \quad (\text{A14})$$

Specifically, $I_3(\omega)$ is given by

$$I_3(\omega) = \frac{|\bar{s}_1|^2 - \bar{s}_2}{\mu_1} + \frac{\Omega^2(\bar{s}_1^*)^2 - \Omega^2(|\bar{s}_1|^2 - \bar{s}_2)\mu_2/\mu_1 - 2i\Omega\bar{s}_1^*\bar{s}_2\mu_2}{2\mu_1\mu_2\mu_3 + \Omega^2(\mu_1 + \mu_2)}, \quad (\text{A15})$$

where $\mu_1 = -\Gamma_2 + i\delta\omega_{01}$, $\mu_2 = -\Gamma_2 + i(\omega + \omega_{01} - 2\omega_p)$, and $\mu_3 = -\Gamma_1 + i\delta\omega_{01}$ with $\delta\omega_{01} = \omega - \omega_{01}$. Combining

the above results, the incoherent part of the spectrum is obtained as

$$S_i(\omega) = \frac{\Gamma_r}{\pi} \text{Re}[I_3(\omega)], \quad (\text{A16})$$

which is the same as Ref [52].

When the pump is on resonance with the qubit, if the pump power is strong ($\Omega \gg \Gamma_{1,2}$), $s_2 \approx \frac{1}{2}$ and $s_1 \approx \frac{-i\Gamma_1}{2\Omega}$. Then, $I_3(\omega)$ can be simplified to

$$\begin{aligned} I_3(\omega) &\approx -\frac{1}{4\mu_1} - \frac{1}{4\mu_1} \frac{\mu_3 + \Gamma_1}{\mu_1\mu_3 + \Omega^2} \\ &\approx -\frac{1}{4\mu_1} - \frac{1}{4} \left\{ \frac{1}{\Gamma_s + i(\delta\omega_{01} + \Omega)} + \frac{1}{\Gamma_s + i(\delta\omega_{01} - \Omega)} \right\} \end{aligned} \quad (\text{A17})$$

where $\Gamma_r = \Gamma_1 - \Gamma_n$ and $\Gamma_s = \frac{\Gamma_1 + \Gamma_2}{2}$. Therefore, Eq. (A16) becomes

$$\begin{aligned} S_i(\omega) &\approx \frac{1}{\pi} \frac{\hbar\omega_{01}\Gamma_r}{4} \left\{ \frac{\Gamma_s}{(\delta\omega_{01} + \Omega)^2 + \Gamma_s^2} \right. \\ &\quad \left. + \frac{2\Gamma_2}{(\delta\omega_{01})^2 + \Gamma_2^2} + \frac{\Gamma_s}{(\delta\omega_{01} - \Omega)^2 + \Gamma_s^2} \right\}. \end{aligned} \quad (\text{A18})$$

Appendix B: Asymmetric Mollow triplet

In this section, we explain how dephasing leads to asymmetry in the off-resonant Mollow triplet. For the driven qubit, the states in the dressed-state basis can be written as

$$|n, +\rangle = \sin\theta|g, n+1\rangle + \cos\theta|e, n\rangle, \quad (\text{B1})$$

$$|n, -\rangle = \cos\theta|g, n+1\rangle - \sin\theta|e, n\rangle, \quad (\text{B2})$$

where $|g\rangle$ ($|e\rangle$) is the ground (excited) state of the qubit, n is the number of drive photons, and θ is defined by

$$\tan 2\theta = -\frac{\sqrt{\Delta^2 + \Omega^2}}{\Delta}. \quad (\text{B3})$$

A sketch of the dressed states is shown in Fig. 4(a). To find the transition rates between the dressed states caused by relaxation, i.e., coupling of an environment to σ_x , we calculate the matrix elements

$$\langle n, +|\sigma_x|n+1, +\rangle = \sin\theta \cos\theta, \quad (\text{B4})$$

$$\langle n, -|\sigma_x|n+1, +\rangle = \cos^2\theta, \quad (\text{B5})$$

$$\langle n, +|\sigma_x|n+1, -\rangle = -\sin^2\theta, \quad (\text{B6})$$

$$\langle n, -|\sigma_x|n+1, -\rangle = -\sin\theta \cos\theta. \quad (\text{B7})$$

Thus, Fermi's golden rule gives that the transition rates are

$$\Gamma_{++} \propto \sin^2\theta \cos^2\theta, \quad (\text{B8})$$

$$\Gamma_{+-} \propto \cos^4\theta, \quad (\text{B9})$$

$$\Gamma_{-+} \propto \sin^4\theta, \quad (\text{B10})$$

$$\Gamma_{--} \propto \sin^2\theta \cos^2\theta. \quad (\text{B11})$$

In the case of resonant drive, $\Delta = 0$, we have $\theta = \pi/4$ and all the transition matrix elements are equal.

As illustrated in Fig. 4(b), the transitions caused by relaxation are either between or within the $+$ and $-$ subspaces. Due to energy conservation, the product of the transition rate from the $+$ subspace to the $-$ subspace, Γ_{+-} , and the occupation probability of state this subspace, P_+ , equals the product of the transition rate from the $-$ subspace to the $+$ subspace, Γ_{-+} , and the occupation probability of this subspace, P_- :

$$\Gamma_{+-}P_+ = \Gamma_{-+}P_-. \quad (\text{B12})$$

If the drive is off-resonant, the transition rates are not the same. For $\delta < 0$, we have $\Gamma_{+-} > \Gamma_{-+}$, and for $\delta > 0$, we have $\Gamma_{-+} > \Gamma_{+-}$, i.e., the sideband that is closest to the qubit frequency has the highest transition rate. However, the emission spectrum is still symmetric, since the number of emitted photons in each sideband is given by the product the corresponding occupation probability and transition rate.

The presence of pure dephasing adds an additional term $H_\phi \propto \sigma_z(a + a^\dagger)$, where a and a^\dagger are annihilation and creation operators for a bath, to the interaction Hamiltonian. The effect that this has on the dressed states can be understood by calculating the transition-matrix elements of σ_z between the dressed states. We find

$$\langle n, +|\sigma_z|n, -\rangle = -2\sin\theta \cos\theta. \quad (\text{B13})$$

All matrix elements of σ_z for transitions between states with different number of drive photons are zero. The effect of pure dephasing is thus to cause transitions as sketched in Fig. 4(a) and (b). Both upward and downward transitions are almost equally likely, since the corresponding transition energies are small compared to $k_B T$.

The pure dephasing thus modifies the condition for equilibrium from Eq. (B12) to

$$(\Gamma_{+-} + \Gamma_\phi)P_+ = (\Gamma_{-+} + \Gamma_\phi)P_-. \quad (\text{B14})$$

This means that a non-zero Γ_ϕ pushes the state of the system closer to $P_- = P_+$ than it otherwise would have been. However, since the transition rates corresponding to relaxation remain the same as before, the result is that more photons are emitted at the frequency of the transition with the larger transition rate. This leads to an asymmetric power spectrum, where more photons are emitted in the sideband closest to the qubit frequency than in the sideband furthest away from the qubit frequency.

Appendix C: Reflection coefficient

From the input-output relation, the output coherent field α_{out} is the sum of the incoming coherent field α_{in}

and the field emitted by the atom:

$$\alpha_{\text{out}} = \alpha_{\text{in}} - i\sqrt{\Gamma_r} \langle \sigma_-(t) \rangle, \quad (\text{C1})$$

where $\alpha_{\text{in}} = \frac{\Omega}{2\sqrt{\Gamma_r}}$. Combining this with Eq. (A7), the reflection coefficient, $r = \frac{\alpha_{\text{out}}}{\alpha_{\text{in}}}$, becomes:

$$r = 1 - \frac{i\Gamma_r\Gamma_1(\Delta - i\Gamma_2)}{\Omega^2\Gamma_2 + \Gamma_1(\Delta^2 + \Gamma_2^2)}. \quad (\text{C2})$$

In the case of a weak probe ($\Omega \ll \Gamma_2$), Eq. (C2) becomes

$$r = 1 - \frac{i\Gamma_r}{\Delta + i\Gamma_2}. \quad (\text{C3})$$

For a resonant probe ($\Delta = 0$), Eq. (C3) is simplified to

$$r = 1 - \frac{1}{\frac{\Omega^2}{\Gamma_1\Gamma_r} + \frac{\Gamma_2}{\Gamma_r}}. \quad (\text{C4})$$

Appendix D: Power Dissipation

At resonance ($\Delta = 0$), the input power is given by (setting $\hbar\omega_{01} = 1$)

$$P_{\text{in}} = |\alpha_{\text{in}}|^2 = \Omega^2/(4\Gamma_r). \quad (\text{D1})$$

The output power is a sum of coherent and incoherent contributions:

$$P_{\text{out}} = P_{\text{coh}} + P_{\text{incoh}}, \quad (\text{D2})$$

with

$$P_{\text{coh}} = P_{\text{in}}|r|^2 = \frac{\Omega^2}{4\Gamma_r} \left(1 - \frac{\Gamma_1\Gamma_r}{\Omega^2 + \Gamma_2\Gamma_1}\right)^2, \quad (\text{D3})$$

$$\begin{aligned} P_{\text{incoh}} &= \Gamma_r(\langle \sigma_+\sigma_- \rangle - \langle \sigma_+ \rangle \langle \sigma_- \rangle) \\ &= \frac{\Gamma_r}{2} \frac{\Omega^2(\Gamma_1\Gamma_\phi + \Omega^2)}{(\Gamma_1\Gamma_2 + \Omega^2)^2}. \end{aligned} \quad (\text{D4})$$

In particular, when $\Gamma_\phi \ll \Gamma_1$, we have $P_{\text{incoh}} \simeq 2\Gamma_r\rho_{11}^2$. The net power loss is $P_{\text{loss}} = P_{\text{in}} - P_{\text{coh}} - P_{\text{incoh}}$.

$$P_{\text{loss}} = \Gamma_n \frac{\Omega^2}{2(\Gamma_1\Gamma_2 + \Omega^2)} = \Gamma_n\rho_{11}. \quad (\text{D5})$$

When $\Omega^2 \gg \Gamma_1\Gamma_2$, the qubit is saturated. Then, we have $P_{\text{in}} \approx P_{\text{coh}} \approx \frac{\Omega^2}{4}$, $P_{\text{incoh}} \approx \frac{\Gamma_r}{2}$, and $P_{\text{loss}} \approx \frac{\Gamma_n}{2}$.

-
- [1] Matthias Steffen, David P DiVincenzo, Jerry M Chow, Thomas N Theis, and Mark B Ketchen, “Quantum computing: An ibm perspective,” IBM Journal of Research and Development **55**, 13 (2011).
 - [2] Frank Arute, Kunal Arya, Ryan Babbush, Dave Bacon, Joseph C Bardin, Rami Barends, Rupak Biswas, Sergio Boixo, Fernando GSL Brandao, David A Buell, *et al.*, “Quantum supremacy using a programmable superconducting processor,” Nature **574**, 505 (2019).
 - [3] Rami Barends, Julian Kelly, Anthony Megrant, Andrzej Veitia, Daniel Sank, Evan Jeffrey, Ted C White, Josh Mutus, Austin G Fowler, Brooks Campbell, *et al.*, “Superconducting quantum circuits at the surface code threshold for fault tolerance,” Nature **508**, 500 (2014).
 - [4] Xiu Gu, Anton Frisk Kockum, Adam Miranowicz, Yuxi Liu, and Franco Nori, “Microwave photonics with superconducting quantum circuits,” Physics Reports **718**, 1 (2017).
 - [5] Dibyendu Roy, Christopher M Wilson, and Ofer Firstenberg, “Colloquium: Strongly interacting photons in one-dimensional continuum,” Reviews of Modern Physics **89**, 021001 (2017).
 - [6] O Astafiev, Alexandre M Zagorskin, AA Abdumalikov, Yu A Pashkin, T Yamamoto, K Inomata, Y Nakamura, and JS Tsai, “Resonance fluorescence of a single artificial atom,” Science **327**, 840 (2010).
 - [7] Io-Chun Hoi, Anton F Kockum, Tauno Palomaki, Thomas M Stace, Bixuan Fan, Lars Tornberg, Sankar R Sathyamoorthy, Göran Johansson, Per Delsing, and CM Wilson, “Giant cross-kerr effect for propagating microwaves induced by an artificial atom,” Physical Review Letters **111**, 053601 (2013).
 - [8] Arjan F Van Loo, Arkady Fedorov, Kevin Lalumière, Barry C Sanders, Alexandre Blais, and Andreas Wallraff, “Photon-mediated interactions between distant artificial atoms,” Science **342**, 1494 (2013).
 - [9] Mohammad Mirhosseini, Eunjong Kim, Xueyue Zhang, Alp Sipahigil, Paul B Dieterle, Andrew J Keller, Ana Asenjo-Garcia, Darrick E Chang, and Oskar Painter, “Cavity quantum electrodynamics with atom-like mirrors,” Nature **569**, 692 (2019).
 - [10] Anton Frisk Kockum, Adam Miranowicz, Simone De Liberato, Salvatore Savasta, and Franco Nori, “Ultrastrong coupling between light and matter,” Nature Reviews Physics **1**, 19 (2019).
 - [11] P Forn-Díaz, Juan José García-Ripoll, Borja Peropadre, J-L Orgiazzi, MA Yurtalan, R Belyansky, Christopher M Wilson, and A Lupascu, “Ultrastrong coupling of a single artificial atom to an electromagnetic continuum in the nonperturbative regime,” Nature Physics **13**, 39 (2017).
 - [12] Roman Kuzmin, Nitish Mehta, Nicholas Grabon, Raymond Mencia, and Vladimir E Manucharyan, “Superstrong coupling in circuit quantum electrodynamics,” npj Quantum Information **5**, 20 (2019).
 - [13] Axel Kuhn, Markus Hennrich, and Gerhard Rempe, “Deterministic single-photon source for distributed quantum networking,” Physical Review Letters **89**, 067901 (2002).

- [14] Keith R Motes, Jonathan P Olson, Evan J Rabeaux, Jonathan P Dowling, S Jay Olson, and Peter P Rohde, “Linear optical quantum metrology with single photons: exploiting spontaneously generated entanglement to beat the shot-noise limit,” *Physical Review Letters* **114**, 170802 (2015).
- [15] Yu Zhou, Zhihui Peng, Yuta Horiuchi, OV Astafiev, and JS Tsai, “Tunable microwave single-photon source based on transmon qubit with high efficiency,” *arXiv preprint arXiv:1905.04032* (2019).
- [16] ZH Peng, SE De Graaf, JS Tsai, and OV Astafiev, “Tuneable on-demand single-photon source in the microwave range,” *Nature Communications* **7**, 12588 (2016).
- [17] Pol Forn-Díaz, CW Warren, CWS Chang, AM Vadiraj, and CM Wilson, “On-demand microwave generator of shaped single photons,” *Physical Review Applied* **8**, 054015 (2017).
- [18] M Pechal, J-C Besse, M Mondal, M Oppliger, S Gasparinetti, and A Wallraff, “Superconducting switch for fast on-chip routing of quantum microwave fields,” *Physical Review Applied* **6**, 024009 (2016).
- [19] Simone Gasparinetti, Marek Pechal, Jean-Claude Besse, Mintu Mondal, Christopher Eichler, and Andreas Wallraff, “Correlations and entanglement of microwave photons emitted in a cascade decay,” *Physical Review Letters* **119**, 140504 (2017).
- [20] Bixuan Fan, Anton F Kockum, Joshua Combes, Göran Johansson, Io-chun Hoi, CM Wilson, Per Delsing, GJ Milburn, and Thomas M Stace, “Breakdown of the cross-kerr scheme for photon counting,” *Physical Review Letters* **110**, 053601 (2013).
- [21] Sankar R Sathyamoorthy, Lars Tornberg, Anton F Kockum, Ben Q Baragiola, Joshua Combes, Christopher M Wilson, Thomas M Stace, and Göran Johansson, “Quantum nondemolition detection of a propagating microwave photon,” *Physical Review Letters* **112**, 093601 (2014).
- [22] Kunihiro Inomata, Zhirong Lin, Kazuki Koshino, William D Oliver, Jaw-Shen Tsai, Tsuyoshi Yamamoto, and Yasunobu Nakamura, “Single microwave-photon detector using an artificial Λ -type three-level system,” *Nature Communications* **7**, 12303 (2016).
- [23] Shingo Kono, Kazuki Koshino, Yutaka Tabuchi, Atsushi Noguchi, and Yasunobu Nakamura, “Quantum non-demolition detection of an itinerant microwave photon,” *Nature Physics* **14**, 546 (2018).
- [24] Baptiste Royer, Arne L Grimsmo, Alexandre Choquette-Poitevin, and Alexandre Blais, “Itinerant microwave photon detector,” *Physical Review Letters* **120**, 203602 (2018).
- [25] Sankar Raman Sathyamoorthy, Thomas M Stace, and Göran Johansson, “Detecting itinerant single microwave photons,” *Comptes Rendus Physique* **17**, 756–765 (2016).
- [26] Jean-Claude Besse, Simone Gasparinetti, Michele C Collodo, Theo Walter, Philipp Kurpiers, Marek Pechal, Christopher Eichler, and Andreas Wallraff, “Single-shot quantum nondemolition detection of individual itinerant microwave photons,” *Physical Review X* **8**, 021003 (2018).
- [27] Huaixiu Zheng, Daniel J Gauthier, and Harold U Baranger, “Waveguide QED: Many-body bound-state effects in coherent and Fock-state scattering from a two-level system,” *Physical Review A* **82**, 063816 (2010).
- [28] Eduardo Sánchez-Burillo, David Zueco, Luis Martín-Moreno, and Juan José García-Ripoll, “Dynamical signatures of bound states in waveguide QED,” *Physical Review A* **96**, 023831 (2017).
- [29] Giuseppe Calajó, Yao-Lung L Fang, Harold U Baranger, Francesco Ciccarello, *et al.*, “Exciting a bound state in the continuum through multiphoton scattering plus delayed quantum feedback,” *Physical review letters* **122**, 073601 (2019).
- [30] Vanessa Paulisch, HJ Kimble, and Alejandro González-Tudela, “Universal quantum computation in waveguide qed using decoherence free subspaces,” *New Journal of Physics* **18**, 043041 (2016).
- [31] Huaixiu Zheng, Daniel J Gauthier, and Harold U Baranger, “Waveguide-QED-based photonic quantum computation,” *Physical review letters* **111**, 090502 (2013).
- [32] Emanuel Knill, Raymond Laflamme, and Gerald J Milburn, “A scheme for efficient quantum computation with linear optics,” *Nature* **409**, 46 (2001).
- [33] P. Y. Wen, K.-T. Lin, A. F. Kockum, B. Suri, H. Ian, J. C. Chen, S. Y. Mao, C. C. Chiu, P. Delsing, F. Nori, G.-D. Lin, and I.-C. Hoi, “Large collective Lamb shift of two distant superconducting artificial atoms,” *Physical Review Letters* **123**, 233602 (2019).
- [34] PY Wen, AF Kockum, H Ian, JC Chen, F Nori, and I-C Hoi, “Reflective amplification without population inversion from a strongly driven superconducting qubit,” *Physical Review Letters* **120**, 063603 (2018).
- [35] I-C Hoi, AF Kockum, L Tornberg, A Pourkabirian, G Johansson, Per Delsing, and CM Wilson, “Probing the quantum vacuum with an artificial atom in front of a mirror,” *Nature Physics* **11**, 1045 (2015).
- [36] Clemens Müller, Jürgen Lisenfeld, Alexander Shnirman, and Stefano Poletto, “Interacting two-level defects as sources of fluctuating high-frequency noise in superconducting circuits,” *Physical Review B* **92**, 035442 (2015).
- [37] PV Klimov, Julian Kelly, Z Chen, Matthew Neeley, Anthony Megrant, Brian Burkett, Rami Barends, Kunal Arya, Ben Chiaro, Yu Chen, *et al.*, “Fluctuations of energy-relaxation times in superconducting qubits,” *Physical Review Letters* **121**, 090502 (2018).
- [38] Jonathan J Burnett, Andreas Bengtsson, Marco Scigliuzzo, David Niepce, Marina Kudra, Per Delsing, and Jonas Bylander, “Decoherence benchmarking of superconducting qubits,” *npj Quantum Information* **5**, 9 (2019).
- [39] Steffen Schlör, Jürgen Lisenfeld, Clemens Müller, Alexander Bilmes, Andre Schneider, David P Pappas, Alexey V Ustinov, and Martin Weides, “Correlating decoherence in transmon qubits: Low frequency noise by single fluctuators,” *Physical Review Letters* **123**, 190502 (2019).
- [40] A Dunsworth, A Megrant, C Quintana, Zijun Chen, R Barends, B Burkett, B Foxen, Yu Chen, B Chiaro, A Fowler, *et al.*, “Characterization and reduction of capacitive loss induced by sub-micron josephson junction fabrication in superconducting qubits,” *Applied Physics Letters* **111**, 022601 (2017).
- [41] VSC Manga Rao and Stephen Hughes, “Single quantum-dot Purcell factor and β factor in a photonic crystal waveguide,” *Physical Review B* **75**, 205437 (2007).

- [42] Daniel Y Chu and Seng-Tiong Ho, “Spontaneous emission from excitons in cylindrical dielectric waveguides and the spontaneous-emission factor of microcavity ring lasers,” *JOSA B* **10**, 381 (1993).
- [43] G Lecamp, P Lalanne, and JP Hugonin, “Very large spontaneous-emission β factors in photonic-crystal waveguides,” *Physical Review Letters* **99**, 023902 (2007).
- [44] Toshihiko Baba, Tetsuko Hamano, Fumio Koyama, and Kenichi Iga, “Spontaneous emission factor of a microcavity dbr surface-emitting laser,” *IEEE Journal of Quantum Electronics* **27**, 1347 (1991).
- [45] BR Mollow, “Power spectrum of light scattered by two-level systems,” *Physical Review* **188**, 1969 (1969).
- [46] DM Toyli, AW Eddins, S Boutin, S Puri, D Hover, V Bolkhovskiy, WD Oliver, A Blais, and I Siddiqi, “Resonance fluorescence from an artificial atom in squeezed vacuum,” *Physical Review X* **6**, 031004 (2016).
- [47] SM Ulrich, S Ates, S Reitzenstein, A Löffler, A Forchel, and P Michler, “Dephasing of triplet-sideband optical emission of a resonantly driven inas/gaas quantum dot inside a microcavity,” *Physical review letters* **106**, 247402 (2011).
- [48] C Roy and S Hughes, “Phonon-dressed Mollow triplet in the regime of cavity quantum electrodynamics: excitation-induced dephasing and nonperturbative cavity feeding effects,” *Physical Review Letters* **106**, 247403 (2011).
- [49] Stanley H Autler and Charles H Townes, “Stark effect in rapidly varying fields,” *Physical Review* **100**, 703 (1955).
- [50] S Probst, FB Song, PA Bushev, AV Ustinov, and M Weides, “Efficient and robust analysis of complex scattering data under noise in microwave resonators,” *Review of Scientific Instruments* **86**, 024706 (2015).
- [51] Jens Koch, M Yu Terri, Jay Gambetta, Andrew A Houck, DI Schuster, J Majer, Alexandre Blais, Michel H Devoret, Steven M Girvin, and Robert J Schoelkopf, “Charge-insensitive qubit design derived from the cooper pair box,” *Physical Review A* **76**, 042319 (2007).
- [52] Kazuki Koshino and Yasunobu Nakamura, “Control of the radiative level shift and linewidth of a superconducting artificial atom through a variable boundary condition,” *New Journal of Physics* **14**, 043005 (2012).
- [53] AA Abdumalikov Jr, OV Astafiev, Yu A Pashkin, Y Nakamura, and JS Tsai, “Dynamics of coherent and incoherent emission from an artificial atom in a 1D space,” *Physical Review Letters* **107**, 043604 (2011).
- [54] Chris Macklin, K O’Brien, D Hover, ME Schwartz, V Bolkhovskiy, X Zhang, WD Oliver, and I Siddiqi, “A near-quantum-limited Josephson traveling-wave parametric amplifier,” *Science* **350**, 307 (2015).